9-2020

Volcano Video Data Characterized and Classified Using Computer Vision and Machine Learning Algorithms

Alex J. C. Witsil
Boise State University

Jeffrey B. Johnson
Boise State University

Geoscience Frontiers 11 (2020) 1789–1803

Contents lists available at ScienceDirect

Geoscience Frontiers

journal homepage: www.elsevier.com/locate/gsf

Research Paper

Volcano video data characterized and classified using computer vision and machine learning algorithms

Alex J.C. Witsil *, Jeffrey B. Johnson

Department of Geosciences, Boise State University, Boise, ID, USA

ARTICLE INFO

Handling Editor: Biswajeet Pradhan

Keywords:
Volcano monitoring
Plume exit velocity
Volcano webcam
Image processing
Machine learning
Villarrica

ABSTRACT

Video cameras are common at volcano observatories, but their utility is often limited during periods of crisis due to the large data volume from continuous acquisition and time requirements for manual analysis. For cameras to serve as effective monitoring tools, video frames must be synthesized into relevant time series signals and further analyzed to classify and characterize observable activity. In this study, we use computer vision and machine learning algorithms to identify periods of volcanic activity and quantify plume rise velocities from video observations. Data were collected at Villarrica Volcano, Chile from two visible band cameras located ~17 km from the vent that recorded at 0.1 and 30 frames per second between February and April 2015. Over these two months, Villarrica exhibited a diverse range of eruptive activity, including a paroxysmal eruption on 3 March. Prior to and after the eruption, activity included nighttime incandescence, dark and light emissions, inactivity, and periods of cloud cover. We quantify the color and spatial extent of plume emissions using a blob detection algorithm, whose outputs are fed into a trained artificial neural network that categorizes the observable activity into five classes. Activity shifts from primarily nighttime incandescence to ash emissions following the 3 March paroxysm, which likely relates to the reemergence of the buried lava lake. Time periods exhibiting plume emissions are further analyzed using a row and column projection algorithm that identifies plume onsets and calculates apparent plume horizontal and vertical rise velocities. Plume onsets are episodic, occurring with an average period of ~50 s and suggests a puffing style of degassing, which is commonly observed at Villarrica. However, the lack of clear acoustic transients in the accompanying infrasound record suggests puffing may be controlled by atmospheric effects rather than a degassing regime at the vent. Methods presented here offer a generalized toolset for volcano monitors to classify and track emission statistics at a variety of volcanoes to better monitor periods of unrest and ultimately forecast major eruptions.

1. Introduction

Volcano monitoring requires synthesis and analysis of a diverse range of continuously recorded geophysical data. Seismometers have been and remain the primary component of long-term volcano monitoring (Sparks et al., 2012; Titos et al., 2018) but are often complemented by infrasonic microphones (Johnson and Ripepe, 2011; Fee et al., 2013) and web cameras (Falsaperla and Spampinato, 2003; Patrick et al., 2010; Pallister et al., 2019). A major advantage in joint seismo-acoustic time series analysis is the ability to quantify multiple aspects of eruption dynamics including source location (Petersen and McNutt, 2007; Arrowsmith et al., 2010; Richardson et al., 2014), energy partitioning (Johnson and Aster, 2005; Palacios et al., 2016), and plumbing structure (Battaglia et al., 2019). When available, the activity responsible for the seismo-acoustic signals is assessed through direct observation of video records. For example, manual inspection of video frames related seismic and acoustic source mechanisms to large bubble bursts at Mount Erebus, Antarctica (Gerst et al., 2008; Jones et al., 2008), a seething lava lake at Villarrica, Chile (Palma et al., 2008), explosions at Karymsky, Russia (Johnson, 2007), and rockfalls into the Kilauea crater, Hawaii (Orr et al., 2013). Though video data provide insights into eruptive behavior, manually navigating these data to identify and monitor activity is time intensive and often impractical.

For continuous camera surveillance to serve monitoring agencies, video must be distilled into concise time varying features that characterize volcanic activity (Dürig et al., 2018). Within the last 15 years, focused

* Corresponding author.
E-mail address: alexandermiller@u.boisestate.edu (A.J.C. Witsil).
Peer-review under responsibility of China University of Geosciences (Beijing).

https://doi.org/10.1016/j.gsf.2020.01.016
Received 6 August 2019; Received in revised form 24 November 2019; Accepted 26 January 2020
Available online 21 February 2020

computer vision algorithms have synthesized infrared (IR), visual band, and ultraviolet (UV) imagery to describe eruption characteristics. For example, plume shape, volume, apparent temperature, and other morphological parameters were extracted from IR imagery using a novel puff detection algorithm at Sromboli, Italy (Gaudin et al., 2017) as well as fractal analysis at Stromboli, Italy; Fuego, Guatemala; and Sakurajima, Japan (Tournigand et al., 2018). Similarly, visual band imagery has been synthesized using several analytical techniques. Particle tracking routines have elucidated dome uplift at Santiaguito, Guatemala (Johnson et al., 2008), plume velocities at Holuhraun, Iceland (Witt et al., 2018), and drag zones within volcanic jets at Stromboli, Italy (Taddeucci et al., 2015), while edge detection algorithms have characterized plume volume at Mount Erebus, Antarctica (Witsil and Johnson, 2018) and pulsating vents at Kilauea, Hawaii (Witt et al., 2018). While these studies quantified volcanic behavior, their scientific focus was retrospective, occurring after eruptive episodes. Real time analysis of volcanic eruptions is possible using software suites, which provide critical constraints on plume height, ascent velocity, bulk volume, and aperture (Valade et al., 2014; Dürig et al., 2018). However, input parameters must be precisely tuned before characterizing the observed style of activity. If activity shifts and the software is unable to track the new behavior, the ability for monitoring agencies to identify periods of unrest will diminish.

The scope of this paper is directed toward monitoring agencies who need generalized computer vision algorithms to quantify a variety of emissions and identify periods of volcanic unrest. Our analyses focus on data collected in 2015 at Villarrica Volcano, Chile and include the activity prior to and after the major 3 March paroxysm. We apply two computer vision algorithms to these data to quantify and classify the diverse range of observable activity. Onsets of venting and associated plume rise rates are extracted via a row and column projection method while a blob detection algorithm extracts statistics on the emission color and spatial extent. Plume statistics reflect the intensity and type of observable emissions and can distinguish five modes of activity particular to Villarrica in early 2015. Instances of dark emissions, light emissions, nocturnal glow, cloud cover, and inactivity are autonomously identified using a supervised artificial neural network (ANN). Results from the ANN, along with the features extracted from the two computer vision algorithms, relate to eruption processes and track the observable shifts in behavior surrounding the 3 March paroxysm. Together, the computer vision and machine learning algorithms comprise a novel workflow that may be applied to other volcanic systems and thus provide additional tools for volcano monitors.

1.1. Villarrica background and data

Villarrica hosts a long-lived basaltic andesite lava lake (Palma et al., 2008) that experiences major paroxysmal eruptions every ~20 years (Van Daele et al., 2014). In between major eruptions, activity is dominated by mild strombolian style eruptions and lava flows confined to the crater floor (Palma et al., 2008). Activity just prior to the 3 March 2015 paroxysm included an increase in CO_2 gas concentrations (Aiuppa et al., 2017), more violent strombolian eruptions (Romero et al., 2018) and a rising lava lake (Johnson et al., 2018). The paroxysm initiated with increased strombolian activity that culminated in an hour long 1.5 km high lava fountain, which partially melted the summit glacier causing lahars to descend several drainages (Johnson and Palma, 2015). Afterwards and continuing until late March, lava from the eruption temporarily buried the lava lake (Romero et al., 2018). The diverse volcanic behavior manifested as a range of observed activity including nighttime incandescence and daytime emissions of varying color and intensity, which relate to ambient lighting as well as variations in ash concentrations and gas species. The focus of this study is quantifying and classifying the observable activity above the crater rim as recorded by two different optical camera setups (Fig. 1).

Video data come from two cameras that recorded the activity prior to and after the 3 March 2015 paroxysm. The data are diverse both in terms

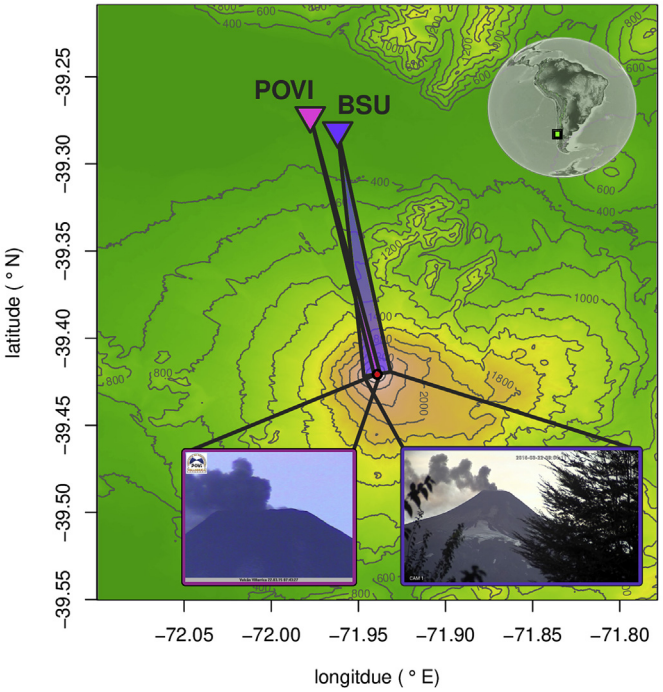

Fig. 1. Cameras used in this study and example frames from those cameras. Field of view (FOV) at Villarrica's crater rim is given for BSU and POVI operated cameras. Example images from both cameras show activity from the same time period (±10 s).

of the variety of recorded activity and instrument specifications. Prior to 3 March, the webcam-style image data come from the privately operated Villarrica Volcano Observation Project (POVI), which monitors summit activity primarily through archival summit observations (reported by local guides) and optical cameras (www.povi.cl). POVI image data are time lapse (ten second interval) and come from a Samsung SCB-2000 web camera equipped with a 240 mm zoom lens (35 mm equivalent) and situated 15 km from the summit (Fig. 1). During low light conditions, the camera automatically switches to a black and white near infrared (NIR) mode. Camera field of view at the target distance of 15 km was 1088 by 843 m corresponding to a horizontal and vertical pixel resolution of 0.6 m per pixel. Following the eruption on 3 March and continuing throughout April, we operated a video camera (30 frames per second) to complement the low frame rate POVI time lapse installation. This camera was a P300ZX 5–50 mm HD surveillance camera with visible and NIR sensitivity in low light conditions and recorded 17 km from the summit. The field of view was 2112 by 1188 m with a horizontal and vertical pixel resolution of 0.91 m per pixel. Summary camera information is provided in Table 1. While the surveillance camera operated at a frame rate capable of extracting velocities from a rising plume (section 3), the less frequently sampled web camera data contain important information on eruptive dynamics including plume area and color and, significantly, was operational in the lead-up to the paroxysm. Plume statistics extracted from the web camera are used in a machine learning routine to autonomously classify the observed activity (section 2).

2. Classifying activity in webcam footage

Autonomous classification through machine learning (ML) algorithms provide a general framework to map input data into discrete categories and is well suited for a variety of geophysical datasets. The majority of volcanological ML research focuses on identifying seismic modes of activity including long period events, tremor, explosions, and hybrid events (Masotti et al., 2008; Curilem et al., 2009; Langer et al., 2009; Malfante et al., 2018; Titos et al., 2018). ML classification of

Table 1
Overview of camera specifications.

Camera operator	Dates	Dist. to crater (km)	Focal length with lens (mm)	Sensor & size	FPS	Resolution at rim (m/pix)	Angular FOV (deg)
POVI	4 Feb – 1 April, 2015	15	240	CCD $^1/_3$"	1/10	0.6	1.3
BSU	3 Mar – 1 April, 2015	17	50	CMOS ⅓"	30	0.9	6.3

volcano infrasound is less common, though acoustic data from Mt Etna, Italy have been used to locate active vents (Cannata et al., 2011) and have been paired with seismic observations to differentiate eruptive activity (Hajian et al., 2019). Volcano video data, though commonly recorded and capable of constraining various modes of activity, has not previously been used in a ML context. In the following sections, we outline a supervised ML workflow that inputs raw video and outputs a discrete class for each frame.

2.1. Data labeling, pre-processing, and feature extraction

We autonomously classify video data by first defining five classes that are commonly observed at Villarrica. Three classes are associated with volcanic activity and include nocturnal glow, light emissions, and dark emissions. Nocturnal glow is defined as the incandescent glow observed above Villarrica's summit at night, while dark and light emissions correspond to the color of material rising above the crater rim (Fig. 2). Classes associated with inactivity include cloud cover, when the region above the rim is obstructed by clouds, and inactivity, where no discernible emission is present during cloudless conditions. Seasonal variations in the atmosphere are expected over this time period and may affect brightness levels in the recorded video. However, these fluctuations should not influence classification by the supervised ML algorithm so long as classes are identified throughout the two-month study period. As such, classes are manually assigned to 2001 randomly selected frames spanning the entire dataset. Inactivity makes up 67% of the total labeled data (1343 frames) while nocturnal glow, dark emissions, light emissions, and cloud cover make up 12%, 9%, 3%, and 9%, respectively.

The three classes associated with volcano activity are influenced by eruptive behavior and extrinsic conditions including the ambient lighting and weather conditions above the rim. Activity can fluctuate in intensity and also shift between classes. For example, light emissions can shift between opaque and semi-transparent and, in some cases, transition to dark emissions over second time scales. Such shifts are likely unrelated to ambient lighting or atmospheric conditions but rather relate to changes in gas composition, ash concentration, or eruptive source mechanisms. Because we are motivated by a volcano monitoring perspective, where tracking changes in behavior is important, we consider it pertinent to classify these modes of activity.

Supervised ML algorithms use features extracted from labeled data to make predictions. Although pixel values from the red, green, and blue (RGB) color channels can be used as inputs, algorithm performance generally improves by reducing image noise and focusing on regions associated with activity. All preprocessing and feature extraction methodologies are accomplished via the freely available R package *imagefx* (Witsil, 2019). First, raw images are cropped to a pixel area that encompass the region associated with activity, which is directly above the vent (Fig. 3 panel b). To enhance color variance associated with volcanic emissions, the best fit planes are subtracted from the red, green, and blue (RGB) color channels; this removes the DC offset and any color gradients from light sources outside the frame (e.g. sun and moon). Emission colors then range from dark (negative) to bright (positive), where daytime activity varies from bright to dark and nocturnal emissions are generally characterized by a bright glow above the crater rim, which fluctuates in intensity and is occasionally overprinted by small bright transients corresponding to the ejection of incandescent ballistics. We normalize bright and dark color regions by taking the absolute value of each RGB channel, which emphasize regions whose color contrast from the mean.

The dominant color contrasting region is identified using a Laplacian of the Gaussian (LoG) blob detection algorithm (e.g. Lindeberg, 1993). The Gaussian filter for the POVI time lapse imagery uses a standard deviation of 20 pixels (~10 m), which acts as a low-pass filter (Fig. 3 panel c). This spatial dimension matches the smallest observable extent of emission activity. The five-pixel Laplacian then converts the filtered image to source (positive) and sink (negative) regions (Fig. 3 panel d) that is then binarized into to black (zero) and white (one) values (Fig. 3 panel e). White blob regions are associated with high color contrasting regions in the original image. While several blobs may exist in one LoG processed image, we identify the blob associated with the highest pixel value in the Gaussian filtered image. The results from the blob detection processing are used to find the color values and index locations that make up the predominant blob within each RGB channel.

Blob regions for each time lapse image are quantified by their color, spatial distribution, and temporal evolution (Fig. 4). The color statistics extracted include the sum, mean, standard deviation, skewness, and kurtosis of the blob pixel values in each of the RGB channels. Spatial statistics record information on the blob shape and distribution and include the blob area as well as the pixel coordinate's mean, standard deviation, skewness, and kurtosis in the horizontal and vertical direction. The temporal evolution of these statistics is important, and its characteristics are exploited by applying a low pass (LP) filter in the time domain. A five-minute running average is applied to emphasize eruptive modes such as minute-duration nocturnal glow or continuous degassing activity that is commonly observed at Villarrica (Palma et al., 2008). Additionally, we take the time derivative of the five-minute averaged statistics to highlight more punctuated emissions, including puffing activity and discrete explosions. Supplementary Table 1 summarizes 126 independent statistics extracted from time lapse imagery for the three different color channels.

Unnecessary statistics do not add to ML predictive capabilities and inhibit the performance of ML algorithms by slowing the run time, overfitting the data, and masking the true variables capable of class identification (Gheyas and Smith, 2010). This *curse of dimensionality* motivates the active research area of feature selection (e.g. Curilem et al.,

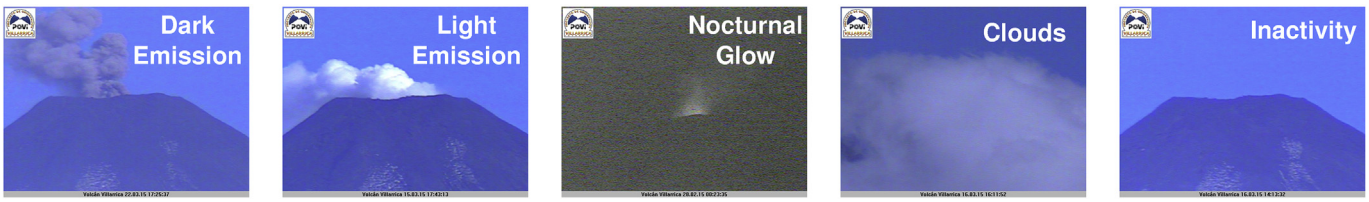

Fig. 2. Examples of the five classes of activity assigned at Villarrica. Dark emission and light emission examples were taken from different days but from the same hour and with similar lighting.

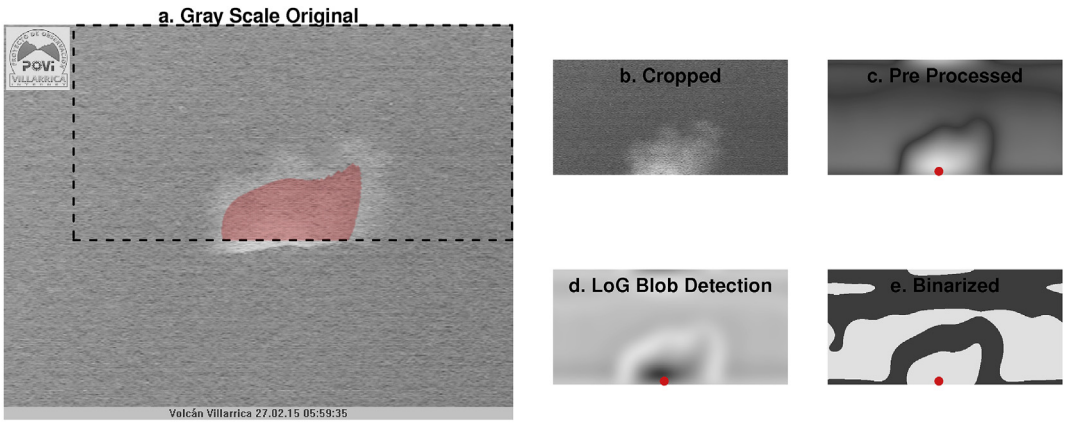

Fig. 3. Overview of image processing. (a) Grayscale original image of nocturnal glow on 27 February 2015. Dashed lines indicate cropped region and red region is result of blob detection algorithm described in the text. (b) Cropped original image. (c) Detrended and gaussian smoothed (σ= 20 pixels) processed image. Red dot indicates the maximum pixel value of this image. (d) Laplacian of the image from panel c. (e) Binarized image of panel d. The blob region is calculated using a connected component algorithm that finds all connected source pixels. This example demonstrates the LoG blob detection algorithm applied to a grayscale image.

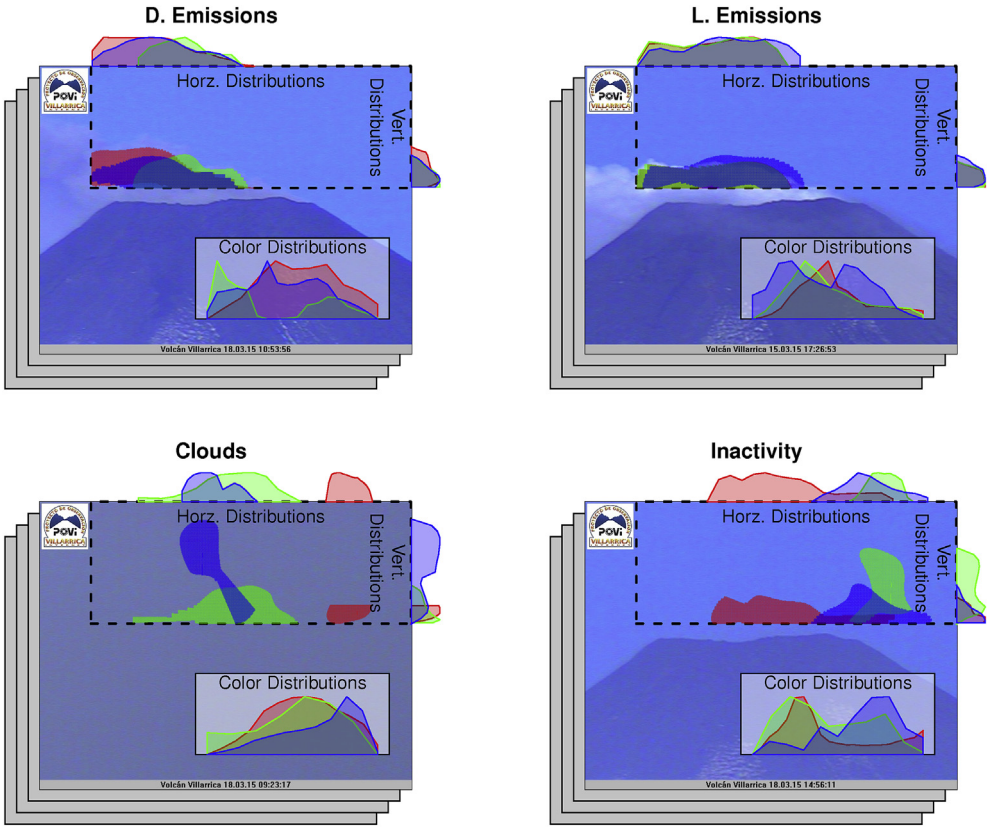

Fig. 4. Blob RGB color and spatial distributions during examples of dark emissions, light emissions, clouds, and inactivity. Blob column and row sums are plotted outside of the top and right margins of the cropped area indicated by the dashed rectangles. Blob RGB histograms are indicated in panel insets. Distribution statistics are calculated for each video frame (stacked gray rectangles).

2009). Therefore, we use a two step process to select a subset of the 126 statistics that are both uncorrelated and also capable of separating the raw data into the five classes. First, statistics that are more than 90% correlated with another statistic are considered redundant and removed from the feature space. Second, we apply the nonparametric Kolmogorov-Smirnov (KS) test over the remaining statistics to compare the five class distributions to the total distribution. The KS test gives the probability that the empirical cumulative distribution function (ECDF) from one class comes from the total distribution (i.e. the ECDF from summing all five classes). Any feature where all five classes have >95% probability of coming from the total distribution are discarded from the feature space (Fig. 5). The correlation analysis and KS test reduces the feature space from 126 to 108 dimensions (see Supplementary Table 1 column 2).

2.2. *Artificial neural network*

Artificial neural networks (ANN) provide a generalized framework to categorize complex signals by emulating the neural connections in animal brains (Van Gerven and Bohte, 2018). In an ANN, one or more values

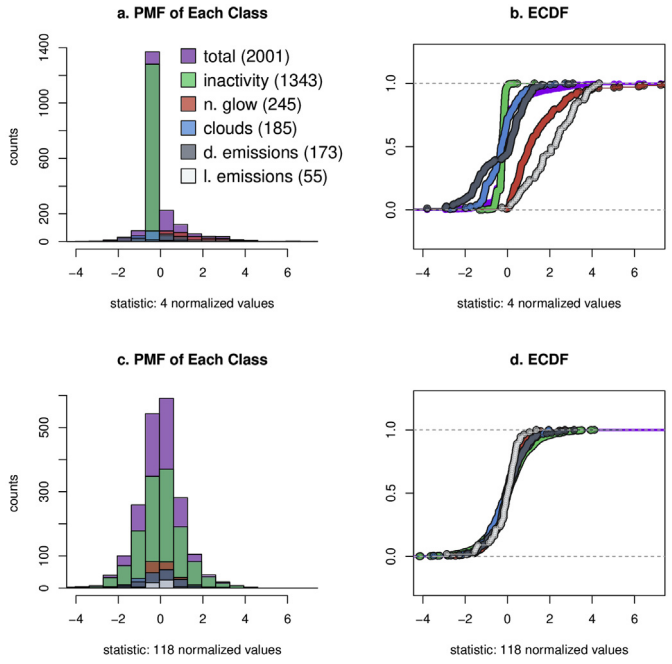

Fig. 5. Class distributions from two example blob features. (a) The total distribution (purple) and each class distribution (remaining colors) of the 4th blob statistic, which corresponds to the mean color values of the blob in the red channel. (b) The empirical cumulative distribution function (ECDF) of (a). Note the separation of each class from the total distribution. (c, d) Histogram and ECDF distributions from the 122nd statistic, which corresponds to kurtosis of the red channel blob's vertical distribution after time differencing and LP filtering. The lack of separation in the ECDF means that this feature failed the KS test and was not used in the ANN.

enter a neuron where they are each weighted, summed, and then input into an activation function whose output can serve as input into another neuron. Outputs from the *j*th neuron (y_j) are determined by a set of input units (u_i) by:

$$y_j = f\left(\sum \Theta_{ij}\, u_i + b_j\right)$$

where, Θ_{ij} is the matrix of neural weights connecting the *i*th unit to the *j*th neuron, b_j is *j*th neuron's bias, and f is the activation function (Falsaperla et al., 1996).

A common ANN framework is the multilayer perceptron (MLP) model (Murphy, 2012), which has been used to classify seismic signals at Mt. Vesuvius, Italy (Scarpetta et al., 2005), Villarrica, Chile (Curilem et al., 2009), Soufriere Hills, Monserrat (Langer et al., 2003), and Stromboli, Italy (Falsaperla et al., 1996). MLPs comprise an input layer of feature data, an output layer where the classification is predicted, and one or more hidden layers (HL) in between (Fig. 6). Each HL comprises one bias node and several additional nodes whose values come from the previous node's activation function. Data are fed-forward through the HLs before reaching the output layer, which has the same number of nodes as classes and whose values indicate the ANN's prediction of which class the input data belong to.

The ANN's performance depends on the weights at each HL and is assessed by comparing the output prediction to the labeled data through a cost function. Cost is backpropagated through the ANN (Rumelhart et al., 1985) to calculate the cost function's gradients. A gradient descent routine then updates each weight to minimize cost and thus best classify the input feature data. This *learning phase* is typically conducted over a subset of the labeled data known as the training set. The ANN's performance also depends on architectural parameters (Curilem et al., 2009) including the number of HLs, number of HL nodes, the regularization term in the cost function, and the optimization routine's learning rate.

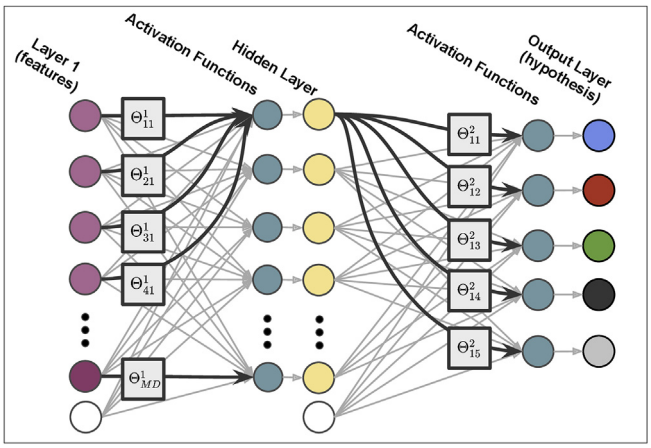

Fig. 6. Example multilayer perceptron (MLP) model of a multi-classification artificial neural network (ANN). The ANN inputs M feature data units and a bias unit (white circle), which together make up the first layer of the ANN. In the case of the POVI webcam data, M = 108 and comes from the selected features from the blob statistics (see section 2.1). Each feature is weighted by the components in matrix Θ whose superscripts indicate the current layer within the ANN. Weighted features are summed and passed to D activation functions whose outputs then serve as new features that are weighted by additional Θ matrices. Herein we use an ANN with D = 108 sigmoid activation functions. A hypothesis is made in the output layer, which, in this case, are the probabilities that the webcam feature data belong to one of the five classes. The entire ANN is fully connected (white arrows) though several connections are highlighted to demonstrate how the Θ weights are applied (bold black arrows).

These parameters must be optimized using a subset of the labeled data that is separate from the training set known as the cross validation (CV) set. The architectural parameters associated with the lowest cost in the CV set are used in the final ANN algorithm whose overall performance is reported using a final subset of the labeled data known as the test set.

The ANN used to classify the webcam images has an input layer consisting of the 108 features that are scaled by subtracting the mean and dividing by the standard deviation. Feature scaling is important when feature values vary widely and helps optimization algorithms, like gradient descent, converge. The ANN uses a sigmoid activation function $f(z) = 1/(1+e^{-z})$ for all layers and a multiclass log loss cost function with regularization parameter λ (Mitchell, 1997). The use of the sigmoid function, as opposed to a softmax function, in the output layer accounts for the possibility that the five classes are not mutually exclusive, and additional classes of activity may exist. This is important if a new style of eruption occurred that was not initially accounted for in the labeled data.

Our goal is to classify webcam footage from Villarrica by training an ANN. The entire learning phase uses a training dataset composing 60% of our labeled data with a gradient descent optimization algorithm running 5000 iterations and with learning rate α. After optimizing the HL weights, we use a CV set composing 20% of the labeled data to optimize the ANN architecture.

We test five HLs between 1 and 5, six HL nodes between 108 and 158, 11 regularization values (λ) between 0 and 10, and five learning rates (α) between 0.001 and 10 and in doing so, test 1650 ANN architectures. The optimum architecture comprises 1 HL, 108 HL nodes, $\alpha = 0.03$, and $\lambda = 0$ and produces a CV cost of 0.380. Because 602 of the 1650 architectures produced similarly low CV costs (less than 1) we conclude that the models performance depends more on the feature inputs and weights rather than the hyperparameters in the ANN's architecture.

2.3. Classification accuracy and application to continuous footage

Frames in the test set are synthesized into the 108 characteristic features and fed-forward through the trained ANN. The sigmoid activation function at the output layer calculates the probabilities that the

current frame belongs to a particular class and the class associated with the highest probability is identified. In doing so, the ANN classifies the test set data into five categories with an overall accuracy of 93%. We further scrutinize the performance of the ANN using a confusion matrix, where properly predicted classes are reported along the diagonal (Table 2).

Nocturnal glow is the most common form of volcanic activity in the labeled dataset and is classified by the ANN with high precision (96%) and recall (96%). Conversely, instances of light emissions make up the minority of labeled data and only 11 examples are included in the test set. As such, the high precision (100%) in this class might not accurately reflect the ANN's performance. Of all the data, cloud identification is least accurate (62% recall and 70% precision) and is most often confused with periods of inactivity. We suggest that cloud identification is most problematic because of their variable shapes, colors, and locations relative to Villarrica's crater rim. Cloud cover during sunrise and sunset may have reddish tones due to increased light scattering. Few instances of sunrise and sunset cloud cover exist in the labeled data meaning that the training data for this class may be inadequate. Additionally, most plumes during the study period were blown from right to left (i.e. west to east) according to the predominant seasonal wind direction (Kalthoff et al., 2002). The ANN may assign too high a weight to the spatial features corresponding to this wind regime. After 23 March, when the predominant wind direction changed, plumes moving from left to right are more likely to be misclassified. To increase the ANN's performance, training data must include labels for all classes occurring over all daily and seasonal atmospheric regimes.

Continuous image data is fed-forward through the trained ANN to classify the entire two-month long webcam dataset. A full day of continuous webcam footage, which is roughly 8000 images at a size of 1.5 GB, is reduced into a single time series summarizing the progression of activity. For example, classified webcam data from 18 February 2015 includes nocturnal glow, dark emissions, cloud cover, and inactivity, which are confirmed during scrutiny of the raw frames (Fig. 7). Between hours 16 and 20, image classification fluctuates between dark emissions, clouds, and inactivity with relatively low associated probabilities for each class. The raw frames during this time (panels e and f) show activity that is hard to identify and exemplifies the ANN's reliance on definitive examples of each class to make predictions with high probabilities.

Two months of webcam data (roughly 90 GB) are synthesized into a stacked time series (aka filled area plot) and show variations in observable activity leading up to, and following, the 3 March 2015 paroxysm (Fig. 8). From mid-February and continuing until March, volcano activity was dominated by inactivity during the day that transitioned to nocturnal glow, which increased in the six days prior to the 3 March paroxysm. In the hour lead-up to, and during, the paroxysm itself, the ANN classified both the increasing strombolian activity and firefountaining phases as nocturnal glow. Though the styles of strombolian and firefountaining activity are different during this period, they were not differentiated as distinct classes because there was too little data to include them in the ANN training phase.

Immediately following the paroxysm, the volcano remained predominately inactive until 13 March when light-colored emissions were observed above the rim during the daylight hours (Fig. 8). These emissions transitioned from light to dark after 18 March. During this period, there was an absence of high amplitude infrasound (Le Pichon et al., 2010; Romero et al., 2018) indicating a departure from Villarrica's normal, open-vent lava lake activity, which produces intense infrasound. The abrupt shift in emission color from light to dark likely relates to remobilized ash ejected from the collapse of lava shelves, which had sealed the crater in the wake of the 3 March eruption. On the night of 24 March, nocturnal glow reappeared and coincides with the reemergence of both recorded volcano infrasound and the previously buried lava lake (Romero et al., 2018).

3. Characterizing plume growth velocities from video

Volcanic plumes comprise the ejected ballistics, ash, and gas as well as ambient air entrained by the eruption column. Plume sizes and growth rates can vary over several orders of magnitude depending on vent geometry, magma flux, magma rheology, and atmospheric conditions. Constraining these parameters with quantitative in-situ observations have significant implications for modeling ash dispersal and forecasting plume-related hazards (e.g. Clarke et al., 2002). In particular, plume exit velocity affects the amount of atmospheric entrainment (Andrews and Gardner, 2009), impacts maximum column height (Caplan-Auerbach et al., 2010), and relates to mass eruption rate (Ripepe et al., 2013). Additionally, at low exit velocities pyroclastic density currents can occur when insufficient air is entrained to produce a buoyant plume (Neri and Dobran, 1994). Horizontal winds also affect plume development; if horizontal wind speeds exceed vertical exit velocities, maximum plume height decreases, and the ash dispersal pattern is asymmetric (Graf et al., 1999; Bursik, 2001; Ripepe et al., 2013). Thus, for monitoring purposes, it is important to track both vertical and horizontal velocities of an expanding plume. Though inferences may be made through seismic (McNutt and Nishimura, 2008; Prejean and Brodsky, 2011; Londono and Galvis Arenas, 2018) and infrasound (Caplan-Auerbach et al., 2010; Ripepe et al., 2013; Delle Donne et al., 2016) signal analysis, they rely on theoretical or empirical relationships with attendant assumptions. More robust measurements can be provided by quantitative measurements of video imagery.

Various IR, UV, and visible light (VL) image datasets permit the measurement of plume and gas exit velocities. Although manual analysis of images was effective in characterizing degassing at Aso, Japan (Morita, 2019), Vulcanian explosions at both Soufriere Hills, Montserrat (Formenti et al., 2003) and Sakurajima, Japan (Johnson and Miller, 2014), and Strombolian eruptions at Stromboli, Italy (Taddeucci et al., 2015), automated tracking of ejecta by computer vision algorithms generalizes the procedure, reduces analysis time, and extends the use of video data as a monitoring tool. Image processing techniques including erosion and dilation (Bombrun et al., 2018), contouring (Donne and Ripepe, 2012; Ripepe et al., 2013), optical flow analysis (Tournigand et al., 2017; Gliß et al., 2018), and fractal analysis (Tournigand et al., 2018) have all been used to track emission velocities in IR and UV spectrums. Other studies have processed VL using edge detection and particle image velocimetry to track firefountaining ejecta at Kilauea, Hawaii (Witt and Walter, 2017)

Table 2
Confusion matrix from the trained ANN applied to the test set. Off-diagonal values ($N = 27$) correspond to inaccurately classified data. Properly classified data on the diagonal ($N = 372$) correspond to 93% of all data. Precision and recall values are given in italics for each class.

Overall accuracy 93%		Predicted					
		Inactivity	N. Glow	D. Emissions	L. Emissions	Clouds	*recall*
Actual	**Inactivity**	258	0	2	0	5	*97*
	N. Glow	1	52	0	0	1	*96*
	D. Emissions	0	0	32	0	3	*91*
	L. Emissions	1	0	1	9	0	*82*
	Clouds	9	2	2	0	21	*62*
	precision	*96*	*96*	*86*	*100*	*70*	

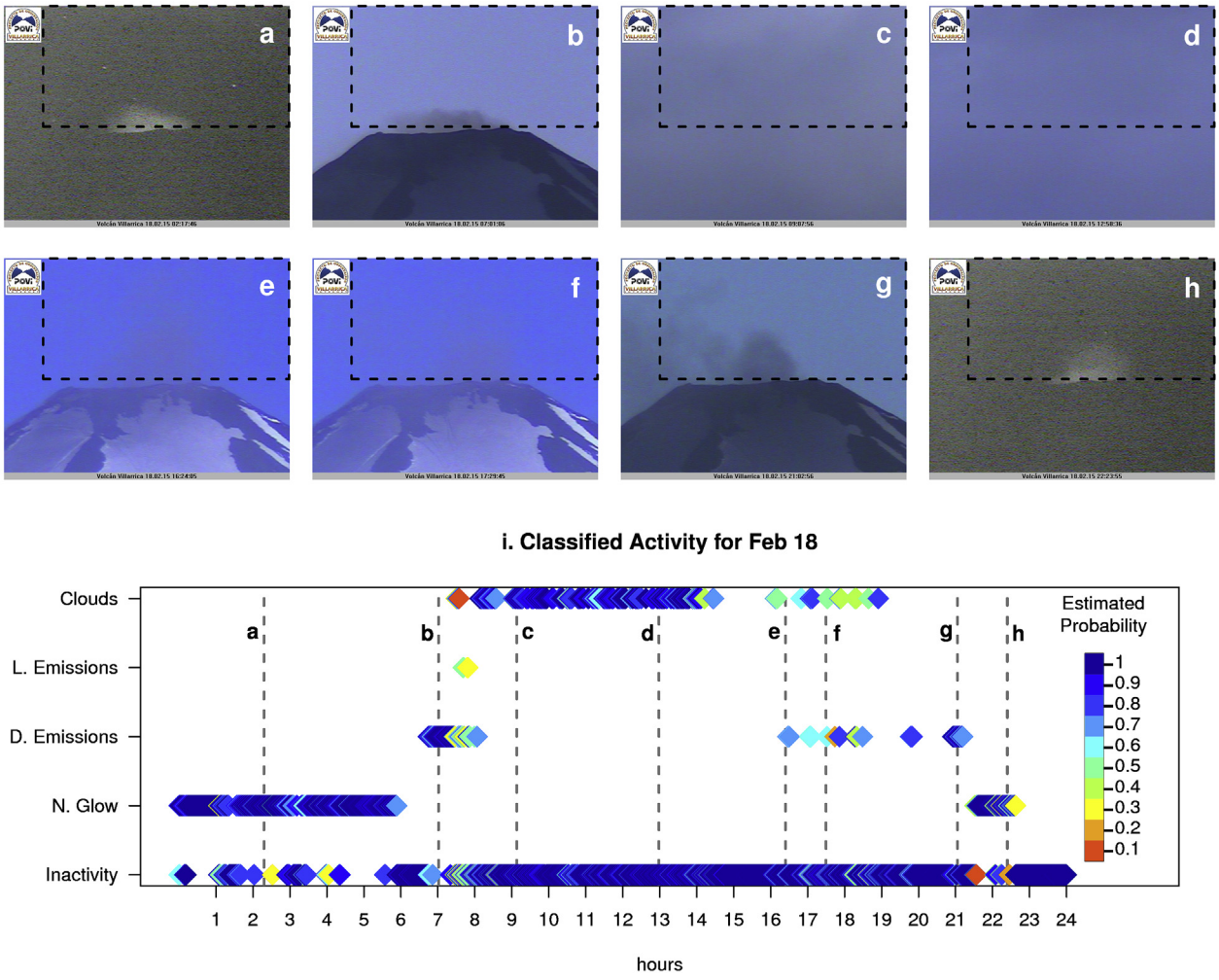

Fig. 7. ANN predictions of activity on 18 February 2015. (a–h) Example video frames from throughout the day. Dashed rectangles indicate the cropped region analyzed. (i) The time series indicate classifications (y axis) for each time step over the 24-h period. Points are color-coded according to the probability of each class given by the ANN. Note, unlike a softmax function, the probabilities from a sigmoid activation function in multi-class classification do not necessarily add to 1.

and Holuhraun, Iceland (Witt et al., 2018), as well as dome uplift at Santiaguito, Guatemala (Johnson et al., 2008). Additionally, thresholding and stacking of VL image frames has been used to track large ballistics at Aso, Japan (Tsunematsu et al., 2019). Because VL image acquisition of eruptions is an inexpensive technology and particularly prevalent at many volcano observatories (Scollo et al., 2014), we introduce some effective tools to both identify plume emissions as well as track the associated horizontal and vertical velocities of a growing plume using Villarrica surveillance camera footage.

3.1. *Plume timing and rise velocity (PTRV) algorithm*

To distill the large volume of surveillance footage at Villarrica into meaningful time series, still frames were first decimated to 1 Hz, converted to grayscale, and cropped to a region centered above the vent. Cropped frames are then preprocessed by subtracting the mean color value and detrending the image by removing the best fit plane. These corrections remove effects due to changes in lighting conditions and light gradients, respectively. Plume features are then highlighted using a row and column projection method (e.g. Pang and Liu, 2001). When a plume is present against a clear (non-cloudy) background, summation of pixel color values along both the rows or columns produce vectors, which emphasize the vertical and horizontal extents of the plume. Successive image row and column sum vectors may then be concatenated into a matrix where columns correspond to time and rows indicate either the column or row sums and are referred to as image series row projections (ISRP) or column projections (ISCP) (e.g., Fig. 9). Similar analyses were performed on successive thermal images at Stromboli, Italy where instead of row summation, the maximum values in each row were retained and plotted (Gaudin et al., 2017). Similar to these thermal rise history diagrams, ISRCPs are visual representations of time varying horizontal and vertical plume features and are an effective way to synthesize hours of video data into one image.

Discrete, or transient, plume emissions are manifested as sloping lineaments (streaks) in the ISRCP records (Fig. 9). In the case where the vent is horizontally centered in the image field of view, a rising volcanic plume first appears in the middle of the ISCP and corresponds to the timing of the plume's emergence above the crater rim. When horizontal winds are present, the plume may be carried either left or right producing streaks in the ISCP with a negative or positive slope (Fig. 9 panel d). In the case where the vent is aligned with the bottom of the cropped image, emergent plumes in the ISRP will be begin in the lower rows and rise with a positive slope, which is proportional to the vertical rise velocity (Fig. 9 panel e).

Processing standard HD video (1920 × 1080 pixel resolution) with ISRP and ISCP reduces its size by three orders of magnitude while maintaining important plume characteristics. Processed video data can then be plotted in time series format, where plume activity is easily discernible and may be quantitatively compared with other datasets. For example, an ISCP spanning 13-h on 22 March shows continuous puffing

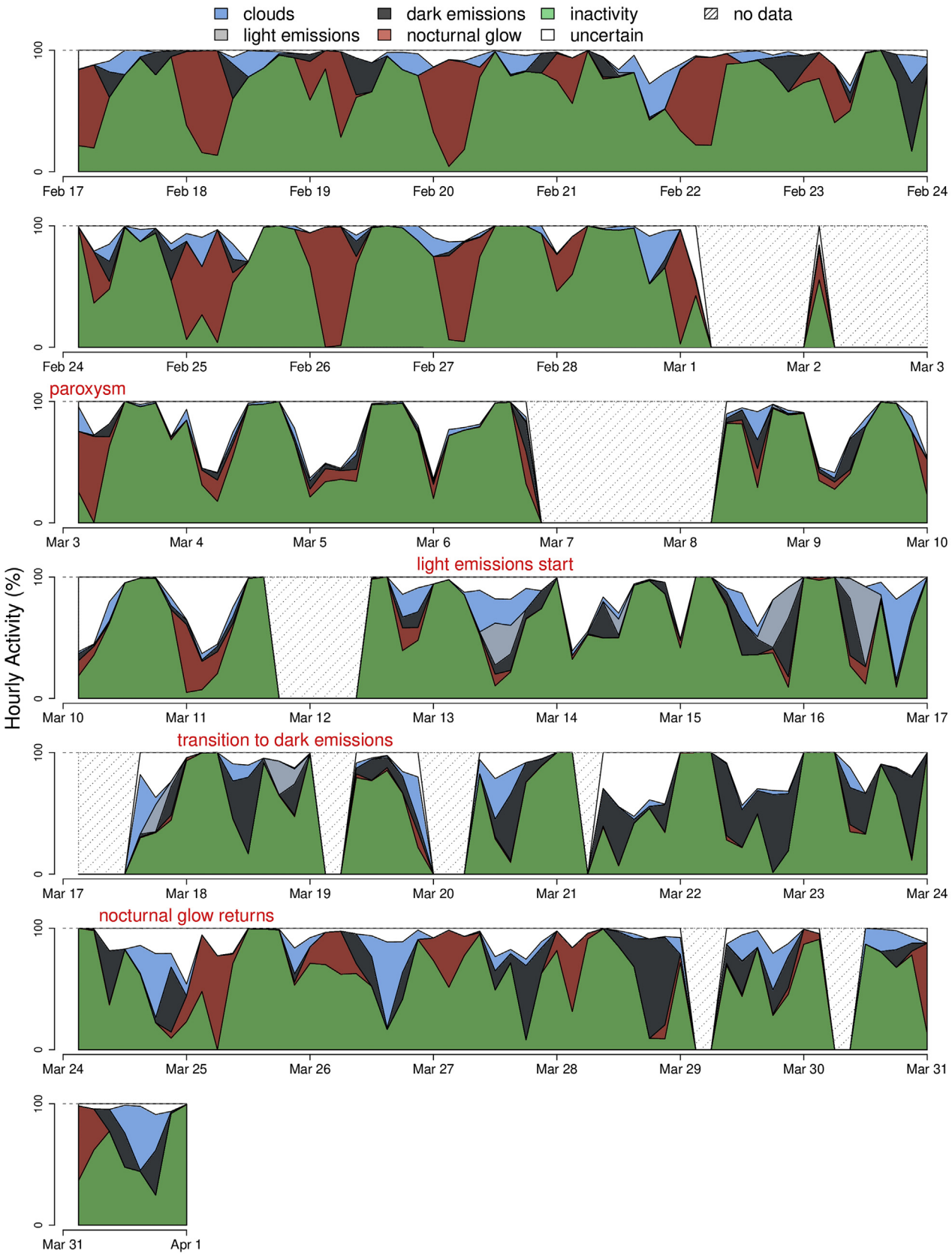

Fig. 8. Chronology of classified activity prior to, and after, the 3 March paroxysm. Predictions from the ANN are indicated for hourly averages. Classifications with less than 80% certainty are labeled as uncertain.

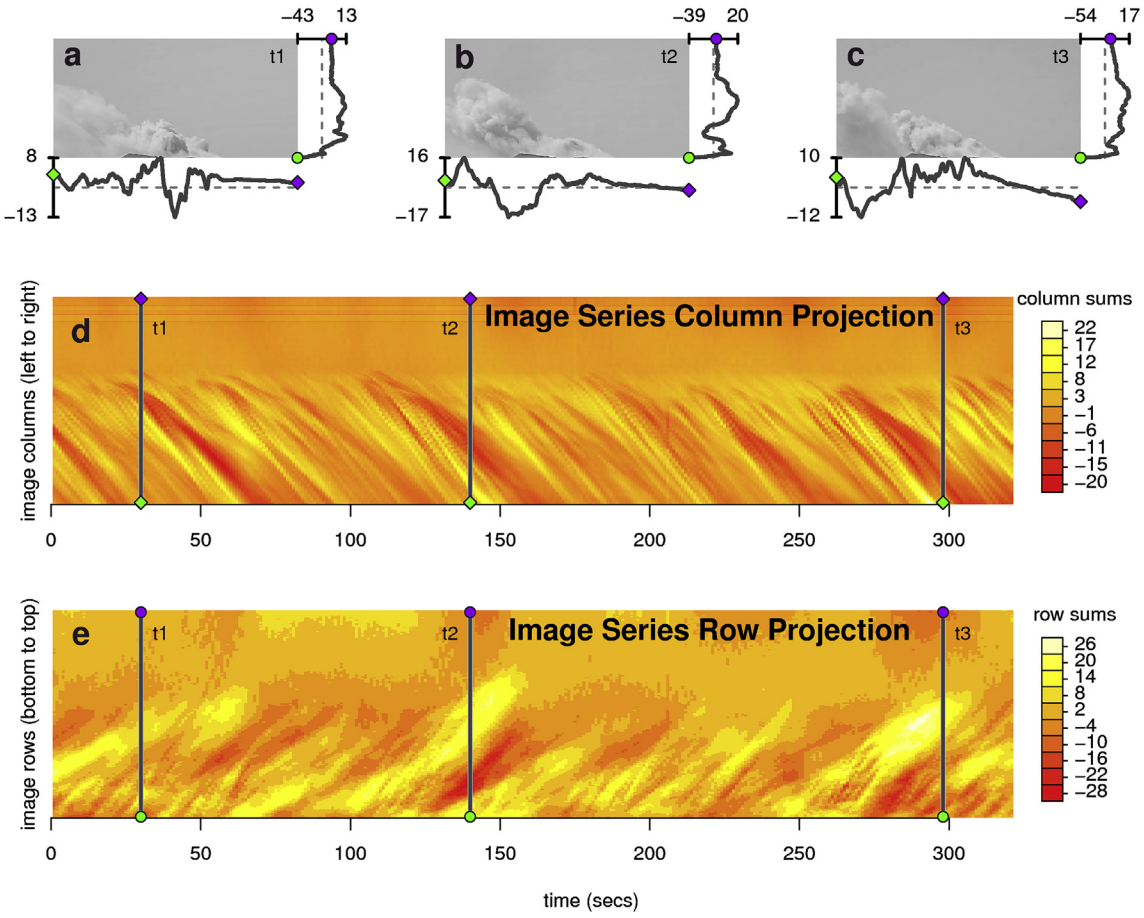

Fig. 9. Visualization of ISCP and ISRP. (a–c) Select still image frames from BSU surveillance footage with row and column sums plotted to the right and below the respective images. Dashed lines indicate the mean value. (d) Column and (e) row sums of ~350 video frames plotted with color corresponding to summed pixel intensity. Vertical lines indicate timing of the image frames in (a–c).

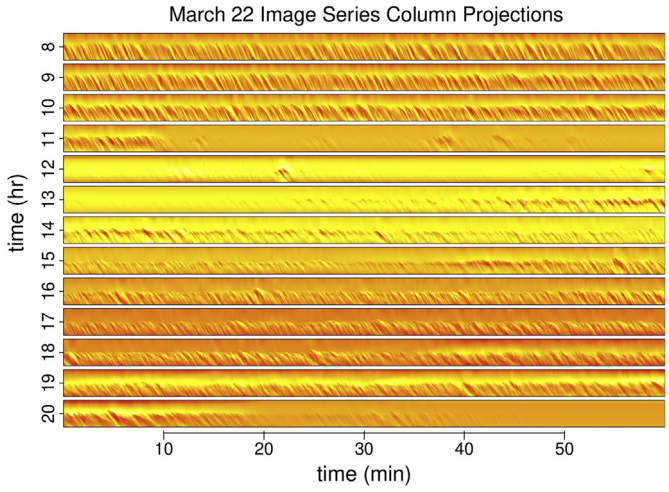

Fig. 10. ISCP for 13-h (local time) of video data from 21 March 2015. Streaks correspond to discrete plume emissions. Colors are scaled every hour.

activity until 11:10, followed by a discrete plume emission at 12:20, and then inactivity until puffing resumes at ~13:30 (Fig. 10).

Streaks in the ISRCPs embody the plume's apparent vertical rise velocities and projected horizontal advection speed. Analysis of ISRCPs can parameterize plume instances and provide important constraints on eruption occurrence and dynamics. Velocities may be extracted from the streak curvature in the ISRCP records, similar to a tau-p analysis in seismic reflection (Turner, 1990). For linear streaks, which are common at Villarrica, a simple slant shift and stack is used to estimate plume velocities; streaks stack in phase after applying the appropriate velocity correction. A proper velocity-corrected ISRP or ISCP matrix will have streaks that appear vertical (panel b in Fig. 11). The summed value of these velocity corrected matrices is referred to here as a plume timing and rise velocity (PTRV) vector, which is calculated independently for both ISCP and ISRP.

The onset of a discrete plume in video records is associated with a sudden change in color level (e.g. bright sky is replaced by dark plume) and these changes can be highlighted in the time domain by applying a running standard deviation operator. For proper velocity-corrected ISCP and ISRP matrices, the PTRV vector will have both high absolute amplitudes and high standard deviations (compare the PTRVs in panel b with panels a and c in Fig. 11). Velocity corrections, corresponding to both vertical plume rise and horizontal advection, are thus found by maximizing standard deviation of the PTRV time series. PTRV vectors may also be used to identify the timing of discrete plume emissions. In the case of ISRP, a sudden change in PTRV marks the emergence of material above the vent, which contrasts with the surrounding atmosphere. Events can be picked based upon whether the PTRV amplitude peaks exceed a certain threshold value (e.g., panel f in Fig. 11).

Horizontal and vertical velocities are tracked by finding the velocity corrections for ISCP and ISRP matrices separately. Absolute plume velocities are then calculated as the square root of the individual squared components $V_{abs} = sqrt(V_{horz}^2 + V_{vert}^2)$. It is important to note that these velocities extracted from integrated ISRCP of a single camera is a pro-

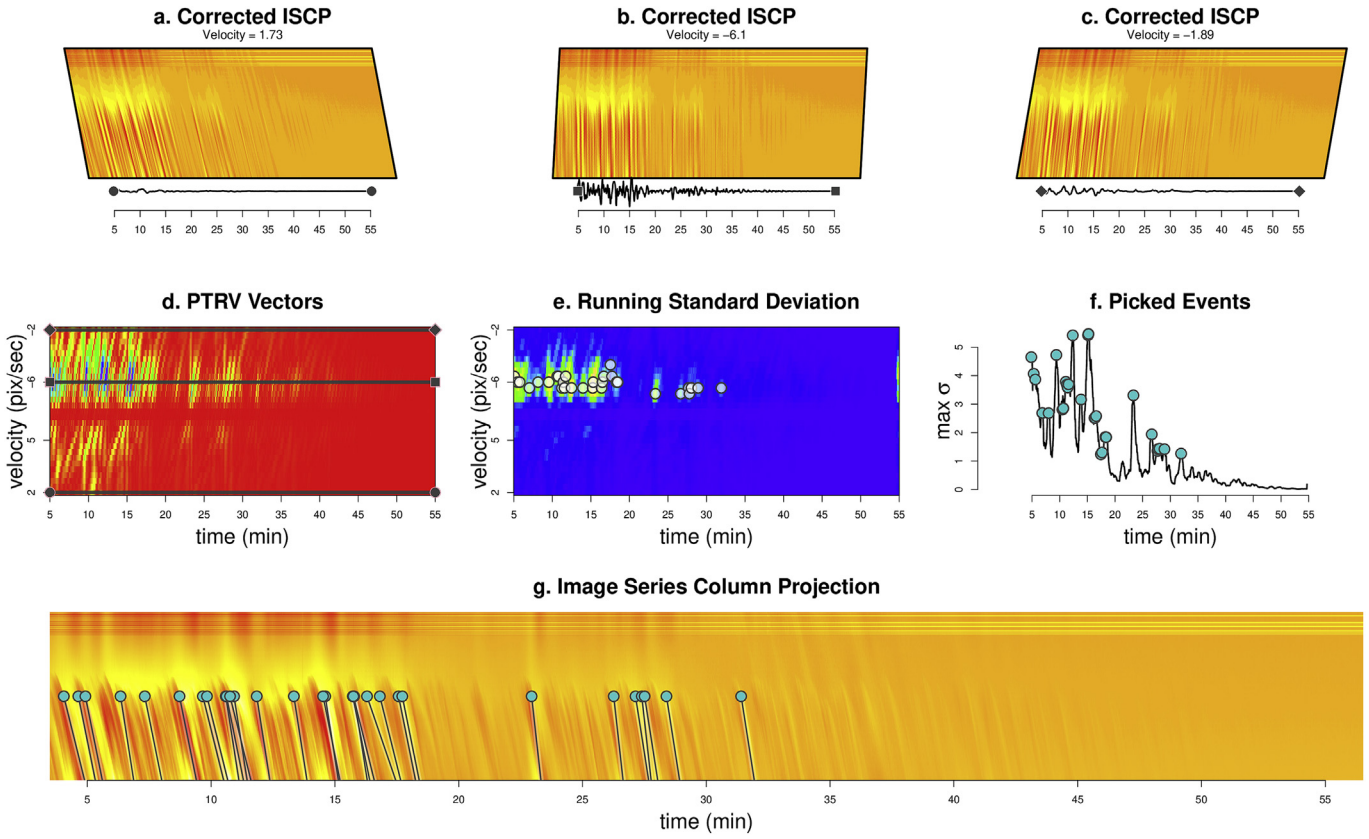

Fig. 11. Overview of plume timing and rise velocity (PTRV) algorithm. (a–c) Example ISCP records corrected over a range of velocities and column summed into PTRV vectors, which are plotted outside the bottom margins. (d) Matrix of PTRV vectors with vector amplitudes plotted as colors. Example vectors from (a–c) are indicated by dark gray lines. (e) Result from applying a running standard deviation to (d). (f) The maximum value from every column in (e). Peaks (teal circles) indicate the timing of plume activity and are found automatically via a find peaks algorithm (see section 3.1) and mapped back to (e) as gray circles. (g) The original ISCP record with plume instances indicated by teal circles and velocities indicated by gray lines.

jected velocity that is perpendicular to the camera's field of view. Multiple cameras located at distinct vantage points could theoretically be integrated to infer a three-dimensional direction of plume growth. Projected plume direction, defined as an angle from vertical, is calculated from the velocity components as $\varphi = atan2(V_{\mathrm{hors}}, V_{\mathrm{vert}})$.

3.2. Characterizing Villarrica puffing with PTRV

The BSU surveillance camera recorded continuously after 3 March 2015 and is particularly useful for tracking and quantifying plume activity after Villarrica's paroxysm. We have applied the PTRV algorithm to nine days in March during which there was minimal cloud cover and episodic occurrences of ash venting. Plume directions and velocities are binned and plotted as rose diagrams for each day (Fig. 12). Strong winds are evident in both measured speeds and in the rose diagram histograms where plume directions are sub-horizontal (March 15–18). A significant change in the wind field from westerlies to easterlies is noticeable starting on 23 March. Wind field quantification through image plume analysis can thus serve as an effective anemometer at the summit of a remote volcano.

The daily number of plume emissions varied between tens to over 600 and indicate a puffing mode of degassing (Palma et al., 2008). Volcanic puffing is generally defined as the discrete, but periodic, emission of volcanic gas or ash over second-long time scales (Harris and Ripepe, 2007; Gaudin et al., 2017), though some studies further stipulate an accompanying acoustic transient from an over pressurized system (Landi et al., 2011; Tamburello et al., 2012). Puffing is both a common and an efficient degassing process (Tamburello et al., 2012) and commonly observed at open vent systems including Yasur, Vanuatu (Bani et al., 2013; Spina et al., 2016), Stromboli, Italy (Ripepe et al., 2009), and Villarrica, Chile (Mather et al., 2004). At Stromboli, Italy the 2007 eruption was preceded by steadily increasing puffing activity, highlighting the need to track and monitor this style of degassing (Ripepe et al., 2009). Though puffing events recorded at Villarrica in March 2015 were observed during periods of low amplitude tremor (coming from the vent direction) (Johnson and Palma, 2015; Johnson et al., 2018), there is no indication that the discrete puffing detected in ISRCP records is correlated with infrasound transients (Fig. 13). We thus suggest that puffing at Villarrica can result from near continuous degassing from the lava lake (tens to hundreds of meters below the crater rim), whose emissions then separate into packets due to horizontal wind effects and vortex shedding.

Vortex shedding occurs when fluid flows past an obstruction and is separated into vortices. It is characterized by the dimensionless Strouhal number $St = fL/U$, where f is the vortex shedding frequency, U is the flow velocity, and L is the characteristic length over which the fluid flows. For flows with Strouhal numbers greater than 10^{-4} and less than 1, oscillations are characterized by the buildup and release of discrete vortices (Sobey, 1982). We estimate Strouhal numbers for a crater rim radius of $L = \sim$150 m and use horizontal wind velocities and plume emission frequencies calculated from the PTRV algorithm that were on average 6.2 m/s and 0.02 Hz, respectively. For 51 periods of puffing identified during 9 days in March $St = 0.5 \pm 0.3$ indicating a regime where periodic vortex shedding is likely to occur. This suggests that the commonly observed puffing activity at Villarrica may result from atmospheric controls, as opposed to periodic degassing from the lava lake surface.

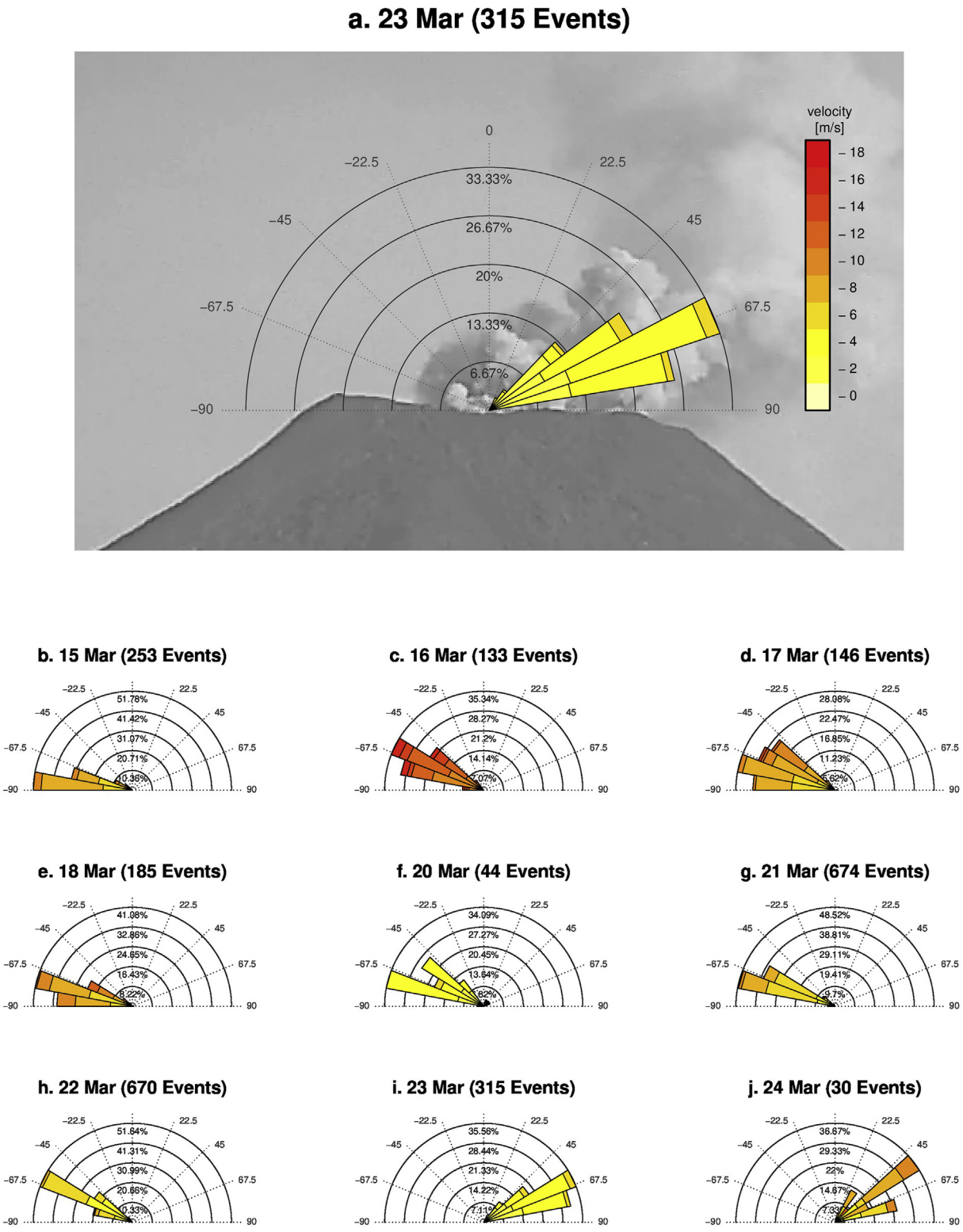

Fig. 12. Plume speeds and directions calculated from PTRV analysis. (a) Rose diagram distribution of plume directions and speeds superimposed on an example grayscale image frame from 23 March 2015. (b–j) Plume growth statistics for nine days in March. Number of events are indicated. Note PTRV analysis is not conducted on 19 March as few plume instances were observed.

4. A generalized video processing workflow

In the previous sections, we outlined methods to classify and characterize a variety of activity at Villarrica Volcano occurring in 2015. We propose these methods can be used conjointly, i.e., classified video frames from the ML algorithm can be used to constrain time periods of sustained emissions, which may then be analyzed with the PTRV algorithm to quantify individual plume emission events. We suggest this generalized workflow of classifying and characterizing periods of activity can be applied to video image data recorded at other volcanoes. In this

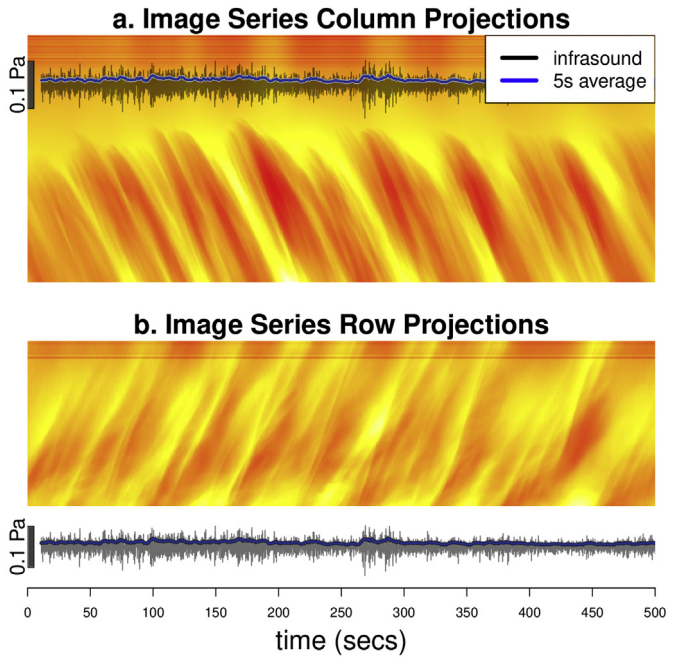

Fig. 13. Example (a) ISCP and (b) ISRP puffing from 21 March, hour 19 plotted with corresponding infrasound recorded ~4 km from the vent. Gray lines correspond to infrasound bandpass filtered between 1 and 10 Hz while bold blue lines show a five second running average applied to the absolute valued infrasound amplitudes. Infrasound has been time shifted ~10 s to align with the video data.

section, we demonstrate the versatility of several processing steps and highlight the modular components within the workflow.

Our classification routine comprises eight steps (Fig. 14), all of which are applicable to a variety of camera deployments with potentially different sensitivities (IR, UV, VL), image acquisition rates, and resolutions. Although other volcano datasets may be trained with greater or fewer classes than those used at Villarrica, activity at any volcano can be labeled according to the analyst's needs. General steps include preprocessing the raw images (i.e., removing the mean and best fit plane within the FOV of interest). High contrast regions with similar color characteristics may then be detected with the LoG blob detection algorithm, which requires adjustment of only a single input parameter, the sigma in the Gaussian LP filter. To demonstrate the value of the blob detection algorithm we have applied it to a range of volcano image datasets, with variable emission colors, shapes, and sizes. Diverse examples from Mount Erebus, Antarctica; Sakurajima, Japan; Santiaguito, Guatemala; and Old Faithful Geyser, Yellowstone were all recorded with different camera instrumentation, FOV, and distances to the vent, yet their emissions are well captured after adjusting the sigma value (Fig. 15). Time scales of eruptive activity, which affect feature quantification, are also different for the various case studies. In the case of Villarrica, the time domain filters highlight the minute-long nocturnal glow activity and the more discrete puffing events, respectively. However, at other volcanoes these filters may have to be adjusted. Feature space reduction may also be particular to individual case studies. In order to avoid redundant features, we remove features that are highly correlated with a somewhat subjective threshold. Finally, parameterization of the ANN is limited to its architecture, whose optimization is described in section 2.2.

The PTRV algorithm can also be applied to a variety of volcano video data so long as the images were acquired at sufficient frame rates to track emissions without aliasing. Long-duration ISRCP records can be used to distill large volumes of video data into a single figure that indicates variations in activity over time. From these data the streak curvature may be used to indicate both plume emission timing and exit speeds. For

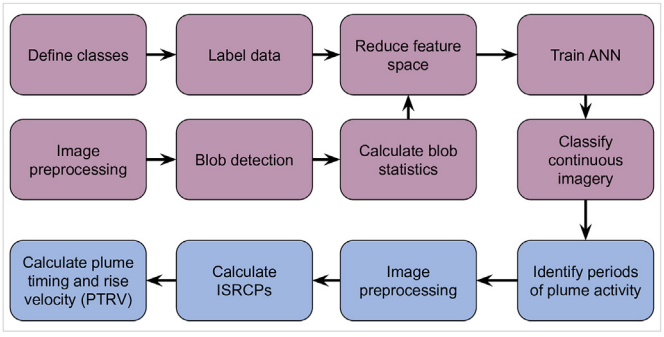

Fig. 14. Workflow of the volcano video classification (pink boxes) and characterization of emissions associated with the PTRV algorithm (blue boxes).

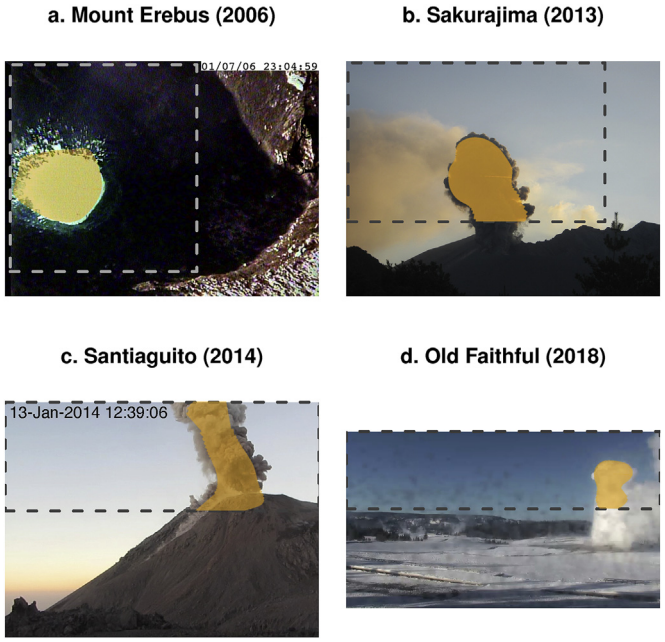

Fig. 15. Eruptions from (a) Mount Erebus, Antarctica, (b) Sakurajima, Japan, (c) Santiaguito, Guatemala, and (d) Old Faithful, Yellowstone and application of LoG blob detection algorithm. Dashed rectangles indicate the manually cropped region for which signals were analyzed.

example, we analyze 14-h of time lapse images from Sakurajima Volcano, Japan, recorded with a GoPro camera located ~4 km from the vent and acquiring images at 10 s intervals. Despite the differences in instrumentation and volcanic activity compared to Villarrica, Sakurajima plume timing and velocities are also well quantified (Fig. 16).

The computer vision workflow presented here provides useful classification and quantification of eruption history, however it is meant to be modular and features from other computer vision algorithms may be easily incorporated depending upon objectives. To give a few examples, plume areas calculated from the LoG blob detection algorithm may be calibrated according to viewing angle and wind direction (e.g. Scollo et al., 2014) and geometric assumptions may be applied to retrieve plume volumes. The ANN we use to classify raw video may be replaced by other ML algorithms used in volcanological studies including support vector machines (Masotti et al., 2008; Langer et al., 2009; Cannata et al., 2011; Curilem et al., 2014), decision trees (Hibert et al., 2017; Hajian et al., 2019), k means (Anzieta et al., 2019), and k nearest neighbors (Orozco-Alzate et al., 2019). Regardless of ML algorithm implementation, a well-chosen feature space is the most important predictor of classification success (Malfante et al., 2018; Hajian et al., 2019). Continuous video acquisition at volcanoes is increasingly common. Versatility and modularity are key to providing

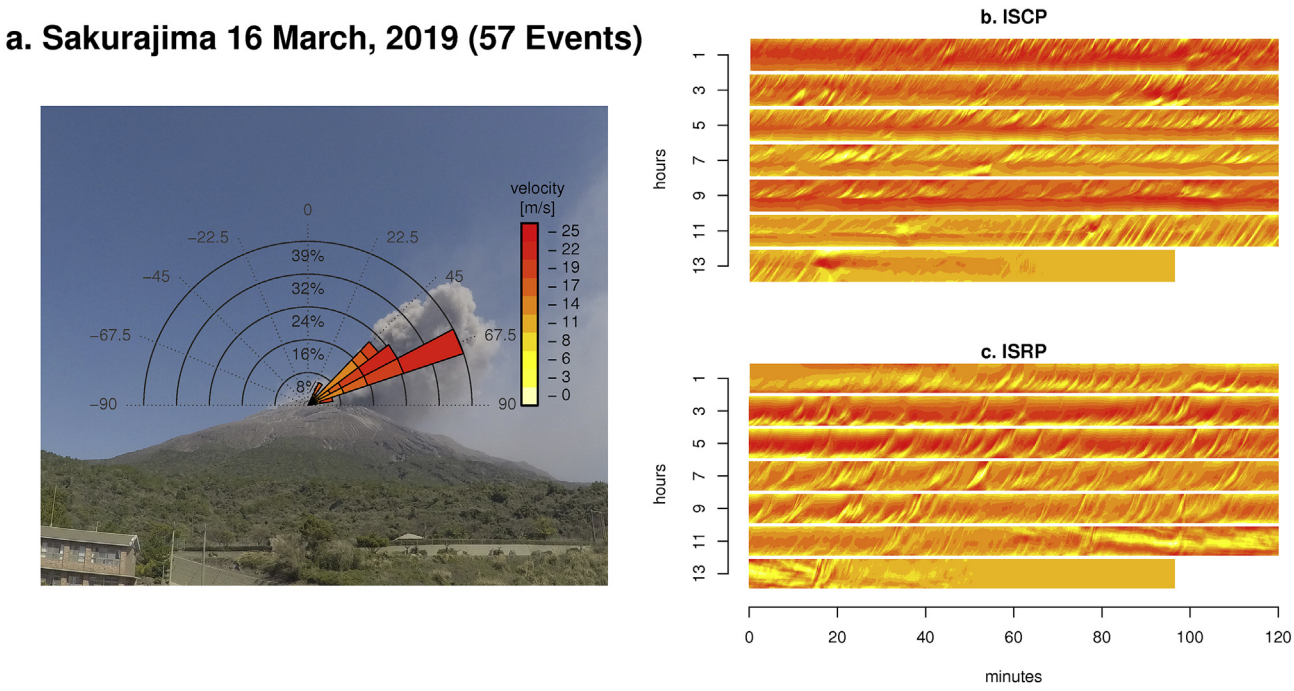

Fig. 16. PTRV algorithm applied to 14-h of video data from Sakurajima Japan. (a) Rose diagram showing plume direction and velocity histogram superimposed on example image frame. (b and c) Corresponding 14-h ISCPs and ISRPs.

video distillation tools that are of value to monitoring agencies and scientific studies.

5. Conclusion

Despite the prevalence of volcano web cameras and other long-term camera installations at volcano observatories, video imagery has only recently been used as a quantitative tool. We apply computer vision and machine learning algorithms to two months of visible band video data collected at Villarrica, Chile to further the scientific merit of long-term video monitoring at volcanoes. The diverse activity surrounding the 3 March paroxysm is classified by an artificial neural network (ANN) that identifies time periods of cloud cover, light emissions, dark emissions, nocturnal glow and inactivity. We are limited by potential subclasses within each mode of activity as well as relatively few instances of cloud cover and light emissions in the training data but nonetheless find the ANN performs with an overall accuracy of 93%. Time periods identified as having plume emissions are further analyzed using a computer vision algorithm (PTRV) that tracks emission timing and growth dynamics from a buoyantly rising plume. Both classification and characterization algorithms compose a generalized and modular workflow that can be modified and applied to other volcanoes with long term camera deployments. Looking forward, researchers should not only continue to develop generalized computer vision and machine learning algorithms but also integrate seismic, acoustic, and other multiparametric data to better constrain eruption dynamics and ultimately improve monitoring and forecasting abilities.

Declaration of competing interest

The authors declare that they have no known competing financial interests or personal relationships that could have appeared to influence the work reported in this paper.

Acknowledgments

This work was made possible through support from Werner Keller and POVI (www.povi.cl) who supplied the webcam data and helpful discussions. E.J. Pettinger from the Boise State University Graduate College assisted with editing and Jacob Anderson and Nicholas Pollock assisted with feedback and insight. Graduate assistantship was partially supported by National Science Foundation grant EAR- 0838562 and EAR-1830976.

Appendix A. Supplementary data

Supplementary data to this article can be found online at https://doi.org/10.1016/j.gsf.2020.01.016.

References

Aiuppa, A., Bitetto, M., Francofonte, V., Velasquez, G., Parra, C.B., Giudice, G., Liuzzo, M., Moretti, R., Moussallam, Y., Peters, N., Tamburello, G., Valderrama, O.A., Curtis, A., 2017. A CO_2-gas precursor to the March 2015 Villarrica Volcano eruption. G-cubed 18 (6), 2120–2132.

Andrews, B., Gardner, J.E., 2009. Turbulent dynamics of the 18 May 1980 Mount St. Helens eruption column. Geology 37, 895–898.

Anzieta, J.C., Ortiz, H.D., Arias, G.L., Ruiz, M.C., 2019. Finding possible precursors for the 2015 Cotopaxi Volcano eruption using unsupervised machine learning techniques. Int. J. Geophys. 2019, 6526898. https://doi.org/10.1155/2019/6526898.

Arrowsmith, S.J., Johnson, J.B., Drob, D.P., Hedlin, M.A., 2010. The seismoacoustic wavefield: a new paradigm in studying geophysical phenomena. Rev. Geophys. 48 (4), RG4003.

Bani, P., Harris, A.J., Shinohara, H., Donnadieu, F., 2013. Magma dynamics feeding Yasur's explosive activity observed using thermal infrared remote sensing. Geophys. Res. Lett. 40 (15), 3830–3835.

Battaglia, J., Hidalgo, S., Bernard, B., Steele, A., Arellano, S., Acuña, K., 2019. Autopsy of an eruptive phase of Tungurahua Volcano (Ecuador) through coupling of seismo-acoustic and SO_2 recordings with ash characteristics. Earth Planet Sci. Lett. 511, 223–232.

Bombrun, M., Jessop, D., Harris, A., Barra, V., 2018. An algorithm for the detection and characterisation of volcanic plumes using thermal camera imagery. J. Volcanol. Geoth. Res. 352, 26–37.

Bursik, M., 2001. Effect of wind on the rise height of volcanic plumes. Geophys. Res. Lett. 28, 3621–3624.

Cannata, A., Montalto, P., Aliotta, M., Cassisi, C., Pulvirenti, A., Privitera, E., Patanè, D., 2011. Clustering and classification of infrasonic events at Mount Etna using pattern recognition techniques. Geophys. J. Int. 185 (1), 253–264.

Caplan-Auerbach, J., Bellesiles, A., Fernandes, J.K., 2010. Estimates of eruption velocity and plume height from infrasonic recordings of the 2006 eruption of Augustine Volcano, Alaska. J. Volcanol. Geoth. Res. 189, 12–18.

Clarke, A., Voight, B., Neri, A., Macedonio, G., 2002. Transient dynamics of vulcanian explosions and column collapse. Nature 415 (6874), 897.
Curilem, G., Vergara, J., Fuentealba, G., Acua, G., Chacón, M., 2009. Classification of seismic signals at Villarrica Volcano (Chile) using neural networks and genetic algorithms. J. Volcanol. Geoth. Res. 180 (1), 1–8.
Curilem, M., Vergara, J., San Martin, C., Fuentealba, G., Cardona, C., Huenupan, F., Chacón, M., Khan, M.S., Hussein, W., Yoma, N.B., 2014. Pattern recognition applied to seismic signals of the Llaima Volcano (Chile): an analysis of the events' features. J. Volcanol. Geoth. Res. 282, 134–147.
Delle Donne, D., Ripepe, M., Lacanna, G., Tamburello, G., Bitetto, M., Aiuppa, A., 2016. Gas mass derived by infrasound and UV cameras: implications for mass flow rate. J. Volcanol. Geoth. Res. 325, 169–178.
Donne, D.D., Ripepe, M., 2012. High-frame rate thermal imagery of strombolian explosions: implications for explosive and infrasonic source dynamics. J. Geophys. Res. 117, B09206 https://doi.org/10.1029/2011JB008987.
Dürig, T., Gudmundsson, M.T., Dioguardi, F., Woodhouse, M., Björnsson, H., Barsotti, S., Witt, T., Walter, T.R., 2018. REFIR- A multi-parameter system for near real-time estimates of plume-height and mass eruption rate during explosive eruptions. J. Volcanol. Geoth. Res. 360, 61–83.
Falsaperla, S., Graziani, S., Nunnari, G., Spampinato, S., 1996. Automatic classification of volcanic earthquakes by using multi-layered neural networks. Nat. Hazards 13 (3), 205–228.
Falsaperla, S., Spampinato, S., 2003. Seismic insight into explosive paroxysms at Stromboli Volcano, Italy. J. Volcanol. Geoth. Res. 125 (1–2), 137–150.
Fee, D., Matoza, R.S., Gee, K.L., Neilsen, T.B., Ogden, D.E., 2013. Infrasonic crackle and supersonic jet noise from the eruption of Nabro Volcano, Eritrea. Geophys. Res. Lett. 40 (16), 4199–4203.
Formenti, Y., Druitt, T., Kelfoun, K., 2003. Characterisation of the 1997 Vulcanian explosions of Soufrière Hills Volcano, Montserrat, by video analysis. Bull. Volcanol. 65 (8), 587–605.
Gaudin, D., Taddeucci, J., Scarlato, P., Harris, A., Bombrun, M., Del Bello, E., Ricci, T., 2017. Characteristics of puffing activity revealed by groundbased, thermal infrared imaging: the example of Stromboli Volcano (Italy). Bull. Volcanol. 79 (3), 24.
Gerst, A., Hort, M., Kyle, P.R., Vöge, M., 2008. 4D velocity of strombolian eruptions and man-made explosions derived from multiple Doppler radar instruments. J. Volcanol. Geoth. Res. 177 (3), 648–660.
Gheyas, I.A., Smith, L.S., 2010. Feature subset selection in large dimensionality domains. Pattern Recogn. 43 (1), 5–13.
Gliß, J., Stebel, K., Kylling, A., Sudbø, A., 2018. Improved optical flow velocity analysis in SO_2 camera images of volcanic plumes – implications for emission-rate retrievals investigated at Mt Etna, Italy and Guallatiri, Chile. Atmos. Meas. Tech. 11 (2), 781–801.
Graf, H.F., Herzog, M., Oberhuber, J.M., Textor, C., 1999. Effect of environmental conditions on volcanic plume rise. J. Volcanol. Geoth. Res. 104, 24309–24320.
Hajian, A., Cannavò, F., Greco, F., Nunnari, G., 2019. Classification of Mt Etna (Italy) volcanic activity by machine learning approaches. Ann. Geophys. 61, 50.
Harris, A., Ripepe, M., 2007. Temperature and dynamics of degassing at Stromboli. J. Geophys. Res.: Solid Earth 112 (B3).
Hibert, C., Provost, F., Malet, J.P., Maggi, A., Stumpf, A., Ferrazzini, V., 2017. Automatic identification of rockfalls and volcano-tectonic earthquakes at the Piton de la Fournaise volcano using a random forest algorithm. J. Volcanol. Geoth. Res. 340, 130–142.
Johnson, J., Aster, R., 2005. Relative partitioning of acoustic and seismic energy during strombolian eruptions. J. Volcanol. Geoth. Res. 148 (3–4), 334–354.
Johnson, J.B., 2007. On the relation between infrasound, seismicity, and small pyroclastic explosions at Karymsky Volcano. J. Geophys. Res.: Solid Earth 112 (B8).
Johnson, J.B., Lees, J.M., Gerst, A., Sahagian, D., Varley, N., 2008. Long-period earthquakes and co-eruptive dome inflation seen with particle image velocimetry. Nature 456, 377, 7220.
Johnson, J.B., Miller, A.J., 2014. Application of the monopole source to quantify explosive flux during vulcanian explosions at Sakurajima Volcano (Japan). Seismol Res. Lett. 85 (6), 1163–1176.
Johnson, J.B., Palma, J.L., 2015. Lahar infrasound associated with Volcan Villarrica's 3 March 2015 eruption. Geophys. Res. Lett. 42 (15), 6324–6331. https://doi.org/10.1002/2015GL065024.
Johnson, J.B., Ripepe, M., 2011. Volcano infrasound: a review. J. Volcanol. Geoth. Res. 206 (3–4), 61–69.
Johnson, J.B., Watson, L.M., Palma, J.L., Dunham, E.M., Anderson, J.F., 2018. Forecasting the eruption of an open-vent volcano using resonant infrasound tones. Geophys. Res. Lett. 45 (5), 2213–2220.
Jones, K.R., Johnson, J.B., Aster, R., Kyle, P.R., McIntosh, W., 2008. Infrasonic tracking of large bubble bursts and ash venting at Erebus Volcano, Antarctica. J. Volcanol. Geoth. Res. 177 (3), 661–672.
Kalthoff, N., Bischoff-Gauß, I., Fiebig-Wittmaack, M., Fiedler, F., Thürauf, J., Novoa, E., Pizarro, C., Castillo, R., Gallardo, L., Rondanelli, R., Kohler, M., 2002. Mesoscale wind regimes in Chile at 30 s. J. Appl. Meteorol. 41 (9), 953–970.
Landi, P., Marchetti, E., La Felice, S., Ripepe, M., Rosi, M., 2011. Integrated petrochemical and geophysical data reveals thermal distribution of the feeding conduits at Stromboli Volcano, Italy. Geophys. Res. Lett. 38 (8).
Langer, H., Falsaperla, S., Masotti, M., Campanini, R., Spampinato, S., Messina, A., 2009. Synopsis of supervised and unsupervised pattern classification techniques applied to volcanic tremor data at Mt Etna, Italy. Geophys. J. Int. 178 (2), 1132–1144.
Langer, H., Falsaperla, S., Thompson, G., 2003. Application of artificial neural networks for the classification of the seismic transients at Soufriere Hills Volcano, Montserrat. Geophys. Res. Lett. 30 (21).
Le Pichon, A., Blanc, E., Hauchecorne, A., 2010. Infrasound Monitoring for Atmospheric Studies. Springer Science & Business Media.
Lindeberg, T., 1993. Detecting salient blob-like image structures and their scales with a scale-space primal sketch: a method for focus-of-attention. Int. J. Comput. Vis. 11 (3), 283–318.
Londono, J.M., Galvis Arenas, B.E., 2018. Seismic data, photographic images and physical modeling of volcanic plumes as a tool for monitoring the activity of Nevado del Ruiz Volcano, Colombia. Front. Earth Sci. 6, 162.
Malfante, M., Mura, M.D., Mars, J., Métaxian, J.-P.I., Macedo, O., Inza, A., 2018. Automatic classification of volcano seismic signatures. J. Geophys. Res.: Solid Earth 123 (12), 10–645.
Masotti, M., Campanini, R., Mazzacurati, L., Falsaperla, S., Langer, H., Spampinato, S., 2008. Tremorec: a software utility for automatic classification of volcanic tremor. G-cubed 9 (4), Q04007. https://doi.org/10.1029/2007GC001860.
Mather, T., Tsanev, V., Pyle, D., McGonigle, A., Oppenheimer, C., Allen, A., 2004. Characterization and evolution of tropospheric plumes from Lascar and Villarrica volcanoes, Chile. J. Geophys. Res.: Atmosphere 109, D21303. https://doi.org/10.1029/2004JD004934.
McNutt, S.R., Nishimura, T., 2008. Volcanic tremor during eruptions: temporal characteristics, scaling and constraints on conduit size and processes. J. Volcanol. Geoth. Res. 178 (1), 10–18.
Mitchell, T.M., 1997. Machine Learning. McGraw Hill.
Morita, M., 2019. Temporal variations of plume activities before the 8 October 2016 eruption of Aso Volcano, Japan, detected by ground-based and satellite measurements. Earth Planets Space 71 (1), 7.
Murphy, K.P., 2012. Machine Learning: a Probabilistic Perspective. MIT press.
Neri, A., Dobran, F., 1994. Influence of eruption parameters on the thermofluid dynamics of collapsing volcanic columns. J. Geophys. Res.: Solid Earth 99 (B6), 11833–11857.
Orozco-Alzate, M., Londoño-Bonilla, J.M., Nale, V., Bicego, M., 2019. Towards better volcanic risk-assessment systems by applying ensemble classification methods to triaxial seismic-volcanic signals. Ecol. Inf. 51, 177–184.
Orr, T.R., Thelen, W.A., Patrick, M.R., Swanson, D.A., Wilson, D.C., 2013. Explosive eruptions triggered by rockfalls at Kilauea Volcano, Hawaii. Geology 41 (2), 207.
Palacios, P.B., Dez, M., Kendall, J.M., Mader, H.M., 2016. Seismicacoustic energy partitioning during a paroxysmal eruptive phase of Tungurahua Volcano, Ecuador. Geophys. J. Int. 205 (3), 1900–1915.
Pallister, J., Papale, P., Eichelberger, J., Newhall, C., Mandeville, C., Nakada, S., Marzocchi, W., Loughlin, S., Jolly, G., Ewert, J., Selva, J., 2019. Volcano observatory best practices (vobp) workshops-a summary of findings and bestpractice recommendations. J. Appl. Volcanol. 8 (1), 2.
Palma, J.L., Calder, E.S., Basualto, D., Blake, S., Rothery, D.A., 2008. Correlations between SO_2 flux, seismicity, and outgassing activity at the open vent of Villarrica Volcano, Chile. J. Geophys. Res.: Solid Earth 113 (B10), B10201.
Pang, G.K., Liu, H.H., 2001. Led location beacon system based on processing of digital images. IEEE Trans. Intell. Transport. Syst. 2 (3), 135–150.
Patrick, M.R., Kauahikaua, J.P., Antolik, L., 2010. Matlab tools for improved characterization and quantification of volcanic incandescence in webcam imagery: applications at Kilauea Volcano, Hawaii. US Geol. Surv. Tech. Methods 13 (A1), 1–16.
Petersen, T., McNutt, S.R., 2007. Seismo-acoustic signals associated with degassing explosions recorded at Shishaldin Volcano, Alaska, 2003–2004. Bull. Volcanol. 69 (5), 527–536.
Prejean, S.G., Brodsky, E.E., 2011. Volcanic plume height measured by seismic waves based on a mechanical model. J. Geophys. Res.: Solid Earth 116, B01306. https://doi.org/10.1029/2010JB007620.
Richardson, J.P., Waite, G.P., Palma, J.L., 2014. Varying seismic-acoustic properties of the fluctuating lava lake at Villarrica Volcano, Chile. J. Geophys. Res.: Solid Earth 119 (7), 5560–5573. https://doi.org/10.1002/2014JB011002.
Ripepe, M., Bonadonna, C., Folch, A., Donne, D.D., Lacanna, G., Marchetti, E., Hoskuldsson, A., 2013. Ash-plume dynamics and eruption source parameters by infrasound and thermal imagery: the 2010 Eyjafjallajokull eruption. Earth Planet Sci. Lett. 366, 112–121.
Ripepe, M., Delle Donne, D., Lacanna, G., Marchetti, E., Ulivieri, G., 2009. The onset of the 2007 Stromboli effusive eruption recorded by an integrated geophysical network. J. Volcanol. Geoth. Res. 182 (3–4), 131–136.
Romero, J.E., Vera, F., Polacci, M., Morgavi, D., Arzilli, F., Alam, M.A., Bustillos, J.E., Guevara, A., Johnson, J.B., Palma, J.L., Burton, M., Cuenca, E., Keller, W., 2018. Tephra from the 3 March 2015 sustained column related to explosive lava fountain activity at Volcán Villarrica (Chile). Front. Earth Sci. 6, 98.
Rumelhart, D.E., Hinton, G.E., Williams, R.J., 1985. Learning Internal Representations by Error Propagation. Institute for Cognitive Science, University of California, San Diego.
Scarpetta, S., Giudicepietro, F., Ezin, E.C., Petrosino, S., Del Pezzo, E., Martini, M., Marinaro, M., 2005. Automatic classification of seismic signals at Mt. Vesuvius Volcano, Italy, using neural networks. Bull. Seismol. Soc. Am. 95 (1), 185–196.
Scollo, S., Prestifilippo, M., Pecora, E., Corradini, S., Merucci, L., Spata, G., Coltelli, M., 2014. Eruption column height estimation of the 2011-2013 Etna lava fountains. Ann. Geophys. 57 (2), S0214. https://doi.org/10.4401/ag-6396.
Sobey, I.J., 1982. Oscillatory flows at intermediate Strouhal number in asymmetric channels. J. Fluid Mech. 125, 359–373.
Sparks, R., Biggs, J., Neuberg, J., 2012. Monitoring volcanoes. Science 335 (6074), 1310–1311.
Spina, L., Taddeucci, J., Cannata, A., Gresta, S., Lodato, L., Privitera, E., Scarlato, P., Gaeta, M., Gaudin, D., Palladino, D.M., 2016. Explosive volcanic activity at Mt. Yasur: a characterization of the acoustic events (9– 12th July 2011). J. Volcanol. Geoth. Res. 322, 175–183.

Taddeucci, J., Alatorre-Ibarguengoitia, M.A., Palladino, D.M., Scarlato, P., Camaldo, C., 2015. High-speed imaging of strombolian eruptions: gaspyroclast dynamics in initial volcanic jets. Geophys. Res. Lett. 42, 6253–6260.
Tamburello, G., Aiuppa, A., Kantzas, E., McGonigle, A., Ripepe, M., 2012. Passive vs. active degassing modes at an open-vent volcano (Stromboli, Italy). Earth Planet Sci. Lett. 359, 106–116.
Titos, M., Bueno, A., García, L., Beñıtez, M.C., Ibañez, J., 2018. Detection and classification of continuous volcano-seismic signals with recurrent neural networks. IEEE Trans. Geosci. Rem. Sens. 57 (4), 1936–1948.
Tournigand, P.Y., Fernández, J.J.P., Taddeucci, J., Perugini, D., Sesterhenn, J., Palladino, D.M., 2018. Time evolution of transient volcanic plumes: insights from fractal analysis. J. Volcanol. Geoth. Res. 371, 59–71.
Tournigand, P.Y., Taddeucci, J., Gaudin, D., Fernández, J.J.P., Del Bello, E., Scarlato, P., Kueppers, U., Sesterhenn, J., Yokoo, A., 2017. The initial development of transient volcanic plumes as a function of source conditions. J. Geophys. Res.: Solid Earth 122 (12), 9784–9803.
Tsunematsu, K., Ishii, K., Yokoo, A., 2019. Transport of ballistic projectiles during the 2015 Aso strombolian eruptions. Earth Planets Space 71 (1), 49.
Turner, G., 1990. Aliasing in the tau-p transform and the removal of spatially aliased coherent noise. Geophysics 55 (11), 1496–1503.
Valade, S., Harris, A.J., Cerminara, M., 2014. Plume ascent tracker: interactive matlab software for analysis of ascending plumes in image data. Comput. Geosci. 66, 132–144.
Van Daele, M., Moernaut, J., Silversmit, G., Schmidt, S., Fontijn, K., Heirman, K., Vandoorne, W., De Clercq, M., Van Acker, J., Wolff, C., Pino, M., Urrutia, R., Roberts, S., Vincze, L., De Batist, M., 2014. The 600 yr eruptive history of Villarrica Volcano (Chile) revealed by annually laminated lake sediments. GSA Bulletin 126 (3–4), 481.
Van Gerven, M., Bohte, S., 2018. Artificial Neural Networks as Models of Neural Information Processing. Frontiers Media SA.
Witsil, A.J., 2019. Imagefx: extract features from images. R package version 0.3.0.
Witsil, A.J., Johnson, J.B., 2018. Infrasound explosion and coda signal investigated with joint analysis of video at Mount Erebus, Antarctica. J. Volcanol. Geoth. Res. 357, 306–320.
Witt, T., Walter, T.R., 2017. Video monitoring reveals pulsating vents and propagation path of fissure eruption during the march 2011 Pu'u'Ō'ō eruption, Kilauea Volcano. J. Volcanol. Geoth. Res. 330, 43–55.
Witt, T., Walter, T.R., Müller, D., Gudmundsson, M.T., Schöpa, A., 2018. The relationship between lava fountaining and vent morphology at the 2014–2015 Holuhraun eruption, Iceland, analysed by video monitoring and topographic mapping. Front. Earth Sci. 6, 235.